

Rotationally invariant distortion resistant finite-elements

Tim Cowan^b, William M. Coombs^a

^a*School of Engineering and Computing Sciences, Durham University
Science Site, South Road, Durham, DH1 3LE, UK.*

T: +44 (0) 191 334 2516, F: +44 (0) 191 334 2408, E: w.m.coombs@durham.ac.uk

^b*BAE systems, Bridge Road, Barrow-in-Furness, LA14 1AF, UK.*

Abstract

The predictive capability of conventional iso-parametric finite-elements deteriorates with mesh distortion. In the case of geometrically non-linear analysis, changes in geometry causing severe distortion can result in negative Jacobian mapping between the local and global systems resulting in numerical breakdown. This paper presents a finite-element formulation that is resistant to irregular mesh geometries and large element distortions whilst remaining invariant to rigid body motion. The predictive capabilities of the family of finite-elements are demonstrated using a series of geometrically non-linear analyses including an elastic cantilever beam and an elasto-plastic double notched specimen.

Keywords:

finite-elements, mesh distortion, geometric non-linearity, elasto-plasticity, shape functions

1. Introduction

Three-dimensional iso-parametric hexahedral elements generally perform best when in the form of right regular cubes. However, in practice, to reproduce irregular geometries this is not possible. Further, it is well known that the accuracy of the finite element solution deteriorates as elements become distorted. Distortion typically occurs when meshing complex curved geometries or when simulating large deformation processes like forging or extrusion. Distorted elements can lead to not just inaccurate results but, in extreme cases, breakdown of the numerical algorithm through a negative Jacobian mapping between the local and global systems. At this point, one is forced down the computationally expensive task of re-meshing and transferring the state variables and internal forces to the new discretisation. The problem of mesh distortion sensitivity has been apparent since the seventies (for example, see [5, 6] amongst others), however a complete solution to the problem has yet to emerge.

Although there have been several alternative approaches to overcoming the distortion sensitivity of finite-elements, such as the smoothed finite-element method [9] and meshless

approaches (see Ullah [22] for an overview), the tremendous popularity of standard finite-elements justifies continued research within this classical framework.

Perhaps the most promising method to produce distortion-*immune* finite elements was introduced by Rajendran and his co-researchers. Rajendran and Liew [17] presented an unsymmetric 8-noded quadrilateral element, reporting that this element could exhibit immunity to any kind of mesh distortion under a quadratic displacement field. They named their new element the US-QUAD8 (unsymmetric quadrilateral element with eight nodes). However, a disadvantage with this formulation is it produces an unsymmetric stiffness matrix requiring an unsymmetric global solver. However, these elements were able to resist mesh distortion and were capable of producing accurate results despite heavy mesh distortion (under certain displacement fields). The element proposed by Rajendran and Liew is only distortion-immune when the underlying basis of the trial functions can exactly capture the displacement field. In this paper we will instead use the term ‘distortion-resistant’ rather than distortion immune.

Ooi *et al* [12] extended the idea of these distortion-resistant unsymmetric elements to three dimensions, proposing an unsymmetric 20-noded hexahedral element (US-HEXA20). Liew, *et al.* [8] introduced a two-dimensional, 6-noded triangular element based on the same underlying formulation. Prathap, *et al.* [15] investigated the approach using the best-fit paradigm. They observed that when an element was distorted, the isoparametric shape functions (used as the test functions) helped satisfy continuity across the element’s edge. Using metric shape functions for the trial basis ensured completeness across the element, allowing exact reproduction of the appropriate order displacement field. This observation explained why the unsymmetric formulation give excellent results for distorted meshes. Another observation made in this paper was the lack of the determinant of the Jacobian matrix in the stiffness integral. This allowed accurate calculations of the stiffness integral, even when the determinant of the Jacobian went negative as a consequence of mesh distortion. However, the Jacobian matrix does feature in the unsymmetric formulation, albeit in an alternative guise.

Rajendran *et al.* [18] further investigated the mesh distortion immunity for the QUAD8 elements using constant, linear and quadratic strain field patch tests. In 2008, Ooi *et al.* [14] highlighted two defects associated with the US-QUAD8. These were its rotational frame dependence and interpolation failure under certain conditions. The remedy to its rotational frame dependence proposed in that paper was given by as rotating the local coordinate system to coincide with one of the element’s edges. Although this did produce a formulation invariant to rigid body rotations, care must be taken to select an appropriate edge. Furthermore, the extension to three-dimensions is not clear. Interpolation failure of the metric shape functions is easy to identify, occurring when the functions do not sum to unity. In cases when this occurred, a random small transformation of the coordinate system was applied, the element constructed and the stiffness matrix was transformed back to its original configuration. Rajendran’s 2010 paper [16] provided a comprehensive study into the 8-noded quadrilateral unsymmetric element formulation. The work extended Prathap

et al.'s [15] studies and investigated how the absence of the Jacobian matrix from the stiffness integral may help reduce inaccuracy due to mesh distortion. The unsymmetric elements of Rajendran and co-workers have also recently been applied to the analysis of finite deformation elastic problems using a total-Lagrangian framework [13].

An alternative to these unsymmetric formulations is the use of hybrid stress-function (HSF) elements (see, for example [2] and the references contained within). HSF elements are based on the principle of minimum complementary energy and their basis functions are obtained from analytical solutions of the Airy stress function. They are able to withstand high mesh distortion and are rotationally invariant. However, a number of points should be noted about these HSF elements: (i) they require significantly higher Gauss-Lagrange quadrature compared to conventional finite-elements and (ii) careful selection of an appropriate number of trial functions is essential to ensure that spurious energy modes do not appear in the element stiffness matrix (this selection process is not yet fully understood [2]). The greatest restriction of the HSF formulation is inherent in the use of Airy stress function solutions, limiting the elements to elastic analyses.

A recent paper by Cen *et al.* [3] proposed an element that combined the unsymmetric approach of Rajendran and co-workers [16, 17] with Cen *et al.*'s [2] HSF formulation. The element overcame the rotational invariance and interpolation failure problems of the unsymmetric formulation by replacing the metric shape function with basis functions from the Airy stress function solution. However, as with the HSF approach, this restricts the element to elastic analysis.

This short paper proposes a new distortion resistant family of finite-elements with a polynomial test and a local convected metric trial basis. The use of a local trial function results in a rotationally invariant element with a clear, clean, implementation for one, two and three-dimensional analysis. The paper also extends the application of these distortion resistant elements to geometrically non-linear elasto-plastic analysis using a total-Lagrangian formulation. For any element to be used in general finite-element analysis, especially in the realm of finite deformation, it is essential that the formulation is invariant to the particular frame of reference.

The layout of the paper is as follows. Section 2 presents the element formulation and provides a clear three-dimensional numerical algorithm. The element is extended to the case of elasto-plastic geometric non-linearity in Section 3. Section 4 presents a series of numerical analyses, namely: (i) a linear elastic plane stress cantilever, (ii) a three-dimensional patch test, (iii) a soft elastic cantilever beam, (iv) an eccentrically loaded column and (v) an elasto-plastic double-notched plate. Finally, brief conclusions are drawn in Section 5. The paper uses a tension positive notation and the equations are mainly presented in matrix-vector format to aid numerical implementation.

2. Element formulation

We restrict the scope of this paper to static stress analysis. The governing weak form of equilibrium can be expressed as a summation of integrals over the problem domain, Ω , and surface, S , as follows

$$\underbrace{\int_{\Omega} [B^L]^T [D^e] [B^R] d\Omega}_{[k^e]} \{d\} = \underbrace{\int_S [N]^T \{t\} dS}_{\{f^{\text{ext}}\}} + \underbrace{\int_{\Omega} [N]^T \{f_b\} d\Omega}_{\{f^b\}}, \quad (1)$$

where $\{f^e\}$ is the internal force vector, $[k^e]$ is the element stiffness matrix, $\{f^{\text{ext}}\}$ is the external force vector, $\{f^b\}$ is a vector containing the nodal body forces and $\{f\}$ is the summation of these two force components. $[B^L]$ and $[B^R]$ are the strain-displacement matrices containing the derivatives of the test and trial shape functions with respect to the global coordinates, $[N]$ contains the test shape functions, $\{t\}$ is the traction vector, $\{d\}$ the element nodal displacements and $[D^e]$ is the elastic material stiffness matrix.

The element stiffness matrix, $[k^e]$, can be approximated through Gauss quadrature as

$$[k^e] = \sum_{i=1}^{n_{Gp}} [B_i^L] [D^e] [B_i^R] \det([J_i]) w_i, \quad (2)$$

where n_{Gp} denotes the number of Gauss points, $[J]$ is the Jacobian matrix and w_i is the weight associated with the Gauss point's location. In three-dimensions the strain-displacement matrices have the following format

$$[B] = \begin{bmatrix} N_{1,x} & 0 & 0 & \dots & N_{n,x} & 0 & 0 \\ 0 & N_{1,y} & 0 & \dots & 0 & N_{n,y} & 0 \\ 0 & 0 & N_{1,z} & \dots & 0 & 0 & N_{n,z} \\ N_{1,y} & N_{1,x} & 0 & \dots & N_{n,y} & N_{n,x} & 0 \\ 0 & N_{1,z} & N_{1,y} & \dots & 0 & N_{n,z} & N_{n,y} \\ N_{1,z} & 0 & N_{1,x} & \dots & N_{n,z} & 0 & N_{n,x} \end{bmatrix}, \quad (3)$$

where N_j denotes the shape function associated with node j and $(\cdot)_{,x}$ denotes the derivative of (\cdot) with respect to x . The classical formulation uses isoparametric shape functions, N , for both the test and trial functions. These interpolation polynomials are formulated in terms of a local coordinate system (ξ, η, ζ) with the requirements that they: (i) sum to one throughout the element and (ii) they equal unity at their associated node and zero at all other nodes. An alternative is to use shape functions that are based on the global coordinates of the elements parent nodes. These *metric* functions can be constructed using a Pascal pyramid, for example for the 20-noded hexahedral element, the metric shape functions at any point within the element (x, y, z) are obtained through rearrangement of

$$\begin{bmatrix}
1 & 1 & \dots & 1 \\
x_1 & x_2 & \dots & x_{20} \\
y_1 & y_2 & \dots & y_{20} \\
z_1 & z_2 & \dots & z_{20} \\
x_1^2 & x_2^2 & \dots & x_{20}^2 \\
y_1^2 & y_2^2 & \dots & y_{20}^2 \\
z_1^2 & z_2^2 & \dots & z_{20}^2 \\
x_1 y_1 & x_2 y_2 & \dots & x_{20} y_{20} \\
x_1 z_1 & x_2 z_2 & \dots & x_{20} z_{20} \\
y_1 z_1 & y_2 z_2 & \dots & y_{20} z_{20} \\
x_1^2 y_1 & x_2^2 y_2 & \dots & x_{20}^2 y_{20} \\
x_1^2 z_1 & x_2^2 z_2 & \dots & x_{20}^2 z_{20} \\
x_1 y_1^2 & x_2 y_2^2 & \dots & x_{20} y_{20}^2 \\
y_1^2 z_1 & y_2^2 z_2 & \dots & y_{20}^2 z_{20} \\
x_1 z_1^2 & x_2 z_2^2 & \dots & x_{20} z_{20}^2 \\
y_1 z_1^2 & y_2 z_2^2 & \dots & y_{20} z_{20}^2 \\
x_1^2 y_1 z_1 & x_2^2 y_2 z_2 & \dots & x_{20}^2 y_{20} z_{20} \\
x_1 y_1^2 z_1 & x_2 y_2^2 z_2 & \dots & x_{20} y_{20}^2 z_{20} \\
x_1 y_1 z_1^2 & x_2 y_2 z_2^2 & \dots & x_{20} y_{20} z_{20}^2 \\
x_1 y_1 z_1 & x_2 y_2 z_2 & \dots & x_{20} y_{20} z_{20}
\end{bmatrix}
\begin{Bmatrix}
M_1 \\
M_2 \\
M_3 \\
M_4 \\
M_5 \\
M_6 \\
M_7 \\
M_8 \\
M_9 \\
M_{10} \\
M_{11} \\
M_{12} \\
M_{13} \\
M_{14} \\
M_{15} \\
M_{16} \\
M_{17} \\
M_{18} \\
M_{19} \\
M_{20}
\end{Bmatrix}
=
\begin{Bmatrix}
1 \\
x \\
y \\
z \\
x^2 \\
y^2 \\
z^2 \\
xy \\
xz \\
yz \\
x^2 y \\
x^2 z \\
xy^2 \\
y^2 z \\
xz^2 \\
yz^2 \\
x^2 yz \\
xy^2 z \\
xyz^2 \\
xyz
\end{Bmatrix}, \quad (4)$$

where the subscript denotes the node number. (4) can be more conveniently expressed as

$$[P]\{M\} = \{p\}. \quad (5)$$

The derivatives of these shape functions with respect to the global coordinates are obtained simply through taking the derivative of $\{p\}$ with respect to each of the coordinate axes and pre-multiplying by the inverse of the element polynomial matrix, $[P]$. For example, the x -direction derivatives are given by

$$\{M_{,x}\} = [P]^{-1} \begin{Bmatrix}
0 \\
1 \\
0 \\
0 \\
2x \\
0 \\
0 \\
y \\
z \\
0 \\
2xy \\
2xz \\
y^2 \\
0 \\
z^2 \\
0 \\
2xyz \\
y^2 z \\
yz^2 \\
yz
\end{Bmatrix}. \quad (6)$$

These derivatives can replace those in (15) to form a metric test or trial strain-displacement

matrix. The unsymmetric distortion resistant formulations proposed in the literature are based on using a polynomial test and global metric trial basis [12, 16, 17, 18, 8].

However, it is well known that these global metric derivatives produce element formulations that are dependent on the orientation of the element. In order to overcome this limitation, Ooi *et al.* [14] proposed that the metric shape functions be reformulated based on a two-dimensional local coordinate system centred on the local coordinate system origin and aligned with one of the element edges. Although this did produce a formulation invariant to rigid body rotations, care must be taken to select an appropriate edge, and the extension to three-dimensions is not clear.

In this paper we propose an alternative procedure where the metric shape functions are based on a convected coordinate system. The derivatives of these local metric interpolation functions are determined through the following procedure:

1. Calculate the position of the Gauss point in the global coordinate system, $\{x_{Gp}\}$, using the conventional polynomial shape functions evaluated at the local Gauss point position, (ξ, η, ζ) , that is

$$\{x_{Gp}\} = \sum_{i=1}^{n_{en}} N_i(\xi, \eta, \zeta) \{x_i\}, \quad (7)$$

where n_{en} is the number of element nodes and $\{x_i\}$ are the nodal coordinates.

2. Determine the rotation matrix between the orientations of the local and global coordinate axes, given by

$$[T] = \begin{bmatrix} \bar{e}_x^r & \bar{e}_x^s & \bar{e}_x^t \\ \bar{e}_y^r & \bar{e}_y^s & \bar{e}_y^t \\ \bar{e}_z^r & \bar{e}_z^s & \bar{e}_z^t \end{bmatrix}, \quad (8)$$

where $\{\bar{e}^r\}$, $\{\bar{e}^s\}$ and $\{\bar{e}^t\}$ are the normalised orientations of the local convected coordinate axes in the global system. These directions are obtained through

$$\{\bar{e}^t\} = \frac{\{x, \zeta\}}{|\{x, \zeta\}|_2}, \quad \{\bar{e}^r\} = \frac{\{x, \eta\} \times \{\bar{e}^t\}}{|\{x, \eta\} \times \{\bar{e}^t\}|_2} \quad \text{and} \quad \{\bar{e}^s\} = \{\bar{e}^t\} \times \{\bar{e}^r\}. \quad (9)$$

$|\{\cdot\}|_2$ denotes the L2-norm of $\{\cdot\}$ and the derivatives of the global coordinates with respect to the local system are obtained from the Jacobian matrix evaluated at the current Gauss point position. That is

$$[J]^T = \begin{bmatrix} \{x, \xi\} & \{x, \eta\} & \{x, \zeta\} \end{bmatrix}, \quad (10)$$

where the Jacobian matrix is obtained from the matrix product of the local coordinate derivatives of the test functions with the global coordinates of the element nodes.

3. Calculate the position of the element nodes, $\{x'_i\}$ in this translated and rotated coordinate system, through

$$\{x'_i\} = \left\{ \{x_i\} - \{x_{Gp}\} \right\} [T]. \quad (11)$$

4. Determine the derivatives of the metric shape functions with respect to the rotated coordinates, $\{M'_{,x}\}$, using (6) with the translated and rotated nodal positions. Note that the Gauss point is located at the origin of the translated and rotated coordinate system, that is $\{x'_{Gp}\} = \{0 \ 0 \ 0\}^T$. This significantly simplifies the vector on the right hand side of (6).
5. Transform the derivatives back into the original system using the rotation matrix linking the global and local axes, through

$$\{M_{,x}\} = \{M'_{,x}\} [T]^T. \quad (12)$$

These derivatives are then used to formulate the strain-displacement matrix (15).

It is worth highlighting that in the proposed mixed formulation, the Jacobian matrix, $[J]$, associated with the conventional parametric shape functions, must be evaluated at each Gauss point position in order to determine the derivatives of the polynomial shape functions with respect to the global coordinate system (in addition to its use in (2)). Therefore, the additional overhead of the local convected metric formulation is associated with determining the global position of the Gauss point and transforming the nodal positions in-to and out-of the local translated and rotated system.

3. Geometric non-linearity

Although the formulation presented in the preceding section provides an element that allows mesh irregularity for linear analysis, a more attractive proposition is in the area of geometrically non-linear analysis where improvements may reduce the need for the computationally expensive task of re-meshing. In this section the key stiffness, internal force and deformation gradient equations for a total-Lagrangian elasto-plastic finite deformation formulation are briefly outlined (for full details of the equivalent parametric updated-Lagrangian formulation see Coombs [4]¹). The formulation described in this paper is based on a logarithmic strain-Kirchhoff stress approach which can be used for isotropic elasto-plastic constitutive models. The use of a logarithmic strain-Kirchhoff stress relationship, in conjunction with an implicit exponential map for the plastic flow equation, allows for the implementation of standard small strain constitutive algorithms within the finite deformation framework without modification. These stress and strain measures provide the basis

¹As noted (and demonstrated through numerical examples) by [1] “*provided that the appropriate constitutive relations are used, the [total and updated Lagrangian] equations yield identical solutions*”.

of the most successful, straightforward ways of implementing large strain elasto-plasticity [7].

The element stiffness matrix for geometrically non-linear analysis can be approximated through Gauss quadrature, as follows

$$[k^e] = \sum_{i=1}^{n_{Gp}} [G_i^L]^T [A] [G_i^R] \det([J_i]) w_i, \quad (13)$$

where $[G^L]$ and $[G^R]$ are the nine-component test and trial tensorial strain-displacement matrices, $[A] = [\partial P / \partial F]$ is the unsymmetric consistent material tangent modulus, $\{P\}$ is the first Piola-Kirchhoff stress vector and $[F]$ is the deformation gradient. The element internal force vector is given by

$$\{f^e\} = \sum_{i=1}^{n_{Gp}} [G_i^L]^T \{P\} \det([J_i]) w_i, \quad (14)$$

where the derivatives of the test and trial functions contained within $[G^L]$ and $[G^R]$ are evaluated in the original, undeformed configuration. The tensorial strain-displacement matrices have the following format

$$[G] = \begin{bmatrix} N_{1,x} & 0 & 0 & \dots & N_{n,x} & 0 & 0 \\ 0 & N_{1,y} & 0 & \dots & 0 & N_{n,y} & 0 \\ 0 & 0 & N_{1,z} & \dots & 0 & 0 & N_{n,z} \\ N_{1,y} & 0 & 0 & \dots & N_{n,y} & 0 & 0 \\ 0 & N_{1,x} & 0 & \dots & 0 & N_{n,x} & 0 \\ 0 & N_{1,z} & 0 & \dots & 0 & N_{n,z} & 0 \\ 0 & 0 & N_{1,y} & \dots & 0 & 0 & N_{n,y} \\ 0 & 0 & N_{1,x} & \dots & 0 & 0 & N_{n,x} \\ N_{1,z} & 0 & 0 & \dots & N_{n,z} & 0 & 0 \end{bmatrix}. \quad (15)$$

Within this geometrically non-linear framework, the deformation gradient provides the fundamental link between the current and the reference configurations for a Lagrangian description of motion

$$[F] = \left[\frac{\partial \{x\}}{\partial \{X\}} \right] = \left[[I] + \frac{\partial \{u\}}{\partial \{X\}} \right], \quad (16)$$

where $\{x\}$ and $\{X\}$ are the coordinates of the same point in the current and reference configurations, respectively, $\{u\}$ is the displacement between the configurations and $[I]$ is the rank three identity matrix. A vector containing the derivatives of the displacement with respect to the original global coordinate can be obtained numerically through

$$\left\{ \frac{\partial \{u\}}{\partial \{X\}} \right\} = [G^R] \{d\} \quad (17)$$

where $\{d\}$ is a vector containing the nodal displacements and $[G^R]$ is evaluated at the point of interest. These components can then be directed into the appropriate locations within (16). The key point to notice from (17), is that the deformation gradient is evaluated using the derivatives of the trial shape functions. The remainder of the finite deformation framework follows the approach of Coombs [4], albeit with a total, rather than updated, description of motion.

4. Numerical capability

This section presents three finite-deformation analyses to demonstrate the capabilities of the proposed formulation. Four different element formulations were investigated, namely:

1. PP: where the classical polynomial shape functions are used for both the test and trial functions;
2. MM: where the global metric shape functions are used for both the test and trial functions;
3. PM: where the polynomial and global metric shape functions are used for the test and trial functions respectively; and
4. PML: where the polynomial and local convected metric shape functions are used for the test and trial functions respectively.

Before presenting the numerical results of this section, it is worth highlighting the numerical results presented by Cen *et al.* [3]. That paper compares the unsymmetric approach of Rajendran and co-workers [16, 17] and Cen *et al.*'s [2] HSF elements with their combined approach through a series of linear analyses. In particular, Cen *et al.* [3] highlight the PM's rotational frame dependence, that has been overcome by the PML formulation, as demonstrated in Sections 4.1 and 4.3 below.

4.1. Plane stress linear cantilever

The first analysis in this paper is a comparison of the approaches of Rajendran and co-workers [16, 17] (PM), Cen *et al.* [2] (HSF-Q8-15 β) and Cen *et al.* [3] (US-ATFQ8) with the PML element proposed in this paper. This plane stress linear elastic cantilever beam problem has been previously analysed by a number of authors [2, 3]. The beam, of length $l_0 = 10\text{m}$ and depth $d_0 = 5\text{m}$, had a Young's modulus of 100Pa and a Poisson's ratio of 0.3 . The cantilever was fully fixed at its root and loaded as shown in Figure 1 (i), with $P = 0.2\text{N}$. Six different discretisations were considered (shown in Figures 1 (i) to (vi)) with $\Delta x_2 = 0.5$, $\Delta x_3 = 3$ and $\Delta x_4 = 3$.

The problem was analysed using the PP, PM and PML (fully integrated eight-noded) formulations under two levels of global clockwise rotation (0° and 20°). The percentage error of the L2 norm of the displacement of node A compared with a reference displacement of 0.054m [2, 3] for these elements, along with the published results of [2, 3], are presented in Table 1.

The PP, PML, HSF-Q8-15 β and US-ATFQ8 formulations are invariant to rigid body rotations whereas the PM element is not. The HSF-Q8-15 β outperforms the other elements, with the exception of mesh (iii) where the US-ATFQ8 has the lowest error. It should be noted that the PML element was able to analyse mesh (vi) containing a concave element whereas the PM element produces a singular stiffness matrix. Also, the results for mesh (v) for the PML element are reported with a very small perturbation of $\delta_x = 1 \times 10^{-12}$ m of two of the meshes nodes (as shown in Figure 1 (v)). Although it is possible to analyse the problem with the PML formulation with $\delta_x = 0$, the stiffness matrix was near singular and the error in the solution was 98.83%.

Although the HSF-Q8-15 β and US-ATFQ8 elements are more accurate than the PML formulation, they are currently limited to linear elastic stress analyses due to the use of Airy stress functions. The rest of the analyses presented in this paper are geometrically non-linear with elastic or elasto-plastic material behaviour.

4.2. Three-dimensional patch test

The first geometrically non-linear simulation is a three-dimensional patch test using the four formulations. The material was taken to be isotropic with a linear elastic relationship between logarithmic strain and Kirchhoff stress. The case of a simple shear deformation field, where the stress throughout the material was constant and could be determined analytically, was investigated, as shown in Figure 2 (i). Eight 20-noded hexahedral elements were used to model the problem. The correct displacement field was imposed on the boundary of the finite-elements, leaving 21 unconstrained degrees of freedom in the interior of the unit cube.

The numerical simulation should result in a constant stress field. The simulations using the four formulations were compared with the analytical solution (see Coombs [4] for derivation of the analytical solution of the Cauchy stress response). As the top face sheared distance Δl increases, initially the shear stress, σ_{zx} , increases before reaching maximum and then softening (as shown in Figure 2 (ii)). The normal stresses σ_{xx} and σ_{zz} are equal in magnitude and opposite in sign with the stress response shown in Figure 2 (ii). Throughout the deformation process $\sigma_{yy} = \sigma_{xy} = \sigma_{yz} = 0$.

For a 1m cube with its top face subsequently sheared by a unit amount in the x -direction (that is $\Delta l = 1m$) and with $E = 1\text{Pa}$ and $\nu = 0.2$, the Cauchy stress throughout the finite-elements should be $\{\sigma\} = \{0.179 \quad 0 \quad -0.179 \quad 0 \quad 0 \quad 0.359\}^T \text{Pa}$. In the case of a uniform finite-element mesh, all of the formulations agreed with the analytical solution. The internal nodes of the mesh were distorted by rotating them about the centre of the element, as shown in Figure 2 (iii) for the case of a rotation about the x -axis of $\theta_x = \pi/6$. Combinations of meshes distorted by $\theta_x \in [0, \pi]$, $\theta_y \in [0, \pi]$ and $\theta_z \in [0, \pi]$ were investigated. The PP, PM and PML formulations produced results invariant to the level of mesh rotation. However, the MM formulation failed the patch test for any amount of mesh rotation, giving stress oscillations through the element.

The case where the internal nodes were randomly displaced by $\in [-0.25, 0.25]$ m in the x , y and z directions was also investigated (as shown in Figure 2 (iv)). Again the PP, PM and PML formulations produced results invariant to the level of mesh distortion, whereas the MM formulation failed to produce the correct uniform stress field.

4.3. Two-dimensional elastic cantilever

This section presents a two-dimensional analysis of a horizontal elastic cantilever beam subjected to a vertical mid-height point load on its free end. The large, moderately soft, deep beam had an original length, l_0 , of 10m and a depth, d_0 , of 1m and was discretised using 40 fully integrated eight-noded plane strain elements, as shown in the top left of Figure 3. The isotropic elastic material had a Young's modulus of 12MPa and a Poisson's ratio of 0.2. The vertical load of 100kN was applied in 50 equal load steps. The end mid-height node force versus normalised displacement response for the undistorted mesh is shown in Figure 3. The final (unexaggerated) deformed configuration is shown in the top left of Figure 3, demonstrating the analysis' large displacements. Reasonable agreement is seen between the numerical simulation and the analytical solution provided by Molstad [10] for both the horizontal and vertical displacements. The four formulations give the same load-displacement response for the undistorted analysis.

In order to test how the formulations performed when elements were distorted, mesh variations were introduced by rotating nodes around a central node at various positions in the mesh. Examples of this distortion are shown in Figure 4, where the degree of rotation is given to the left of the five discretisations. The force versus normalised displacement responses for varying degrees of mesh distortion for the classical PP formulation are shown in Figure 5. Increasing the mesh distortion causes a progressive stiffening, also seen in Table 2. The PP formulation failed to converge at rotations above $5\pi/12$. This was due to overlapping element geometries creating a singular global stiffness matrix. Figure 6 shows the force versus normalised displacement response for the MM formulation. A softening response is observed with increasing levels of mesh distortion. This is also seen in Table 2. However, the formulation was able to withstand significantly more distortion compared to the PP approach; failing at rotations above $9\pi/12$.

The results for the unsymmetric PM formulation show close agreement with the analytical solution for mesh distortions less than $11\pi/12$. The vertical tip displacement was 8.252m for an undistorted mesh and only increased to 8.256m for a mesh distortion of $4\pi/6$, so a slight relaxation of the element was observed. All of the PM load versus normalised displacement responses are indistinguishable from that shown in Figure 3. The local unsymmetric formulation ceased to converge past a mesh distortion rotation of $10\pi/12$. For a mesh distortion of $4\pi/6$ the local unsymmetric formulation had an end mid-node displacement error (in both directions) of less than 0.1% compared with the undistorted PP result (for example, a end mid-node vertical displacement of 8.251m compared with 8.252m). The local unsymmetric element displayed very similar load versus displacement characteristics

to that of the global PM formulation, again indistinguishable from that shown in Figure 3. However, we now globally rotate the $2\pi/6$ distorted discretisation and re-examine the results.

In these rotated analyses the mesh, boundary conditions and external forces were rotated about the global coordinate origin by an angle of between 0 and $\pi/2$ in increments of $\pi/12$. Table 3 presents the normalised vertical and horizontal end, mid-node displacements rotated back into the original coordinate system. It is clear from Table 3 that the PML and PP formulations are frame invariant whereas the displacements obtained from the MM and PM elements are dependent on the frame of reference. The major shortcoming of the metric shape functions has been overcome by recasting them in a convected local coordinate system whilst maintaining the distortion-resistant nature of the antisymmetric element formulation.

4.4. Eccentrically loaded column

This section presents a numerical analysis of an elastic column, of height $l_0 = 10\text{m}$ and width $b_0 = 1\text{m}$, fully fixed at its base and subjected to an eccentric compressive vertical load, P . The geometrically non-linear unit-depth plane strain analysis assumed a Young's modulus of 1MPa and a Poisson's ratio of 0. The column was loaded to four times the critical buckling load $p_{cr} = \pi^2 EI/4l_0^2$ where I is the second moment of area of the square section. Five fully integrated eight-noded quadrilaterals were used to model the column, as shown in Figures 7 (iii) and (iv) for the uniform and distorted meshes respectively. This problem was initially presented by Ooi *et al.* [13] and was used to compare their unsymmetric (PM) formulation with the conventional 8-noded quadrilateral finite-element.

The normalised force versus vertical and horizontal displacement response of the PML and PP formulations are shown in Figures 7 (i) and (ii). Ooi *et al.*'s results for a distorted mesh with $\Delta y = 0.5$ for the PP (circles) and PM (squares) are also shown. Good agreement is observed between the PP results of Ooi *et al.* and those generated in this paper.

With zero mesh distortion the PP and PML results coincide. However, the PP results are highly dependent on the level of mesh distortion. Analyses undertaken using the PML elements shown significantly less mesh-distortion dependence.

4.5. Elasto-plastic double-notched plate

The final analysis is of the stretching of a double-notched plate using the PP, MM and PML formulations. The problem was initially presented by Nagtegaal *et al.* [11] for small strain plasticity to demonstrate the spurious response of standard finite-elements and was subsequently re-analysed in a number of papers [20, 21, 19]. The plate had a Young's modulus of 206.9GPa, Poisson's ratio of 0.29 and was modelled using an exact implementation of the elastic-perfectly plastic Prandtl-Reuss constitutive model [23]. The

yield function for the associated flow model can be expressed as

$$f = \rho^2 - \rho_y^2 = 0, \quad (18)$$

where ρ_y is the yield stress ($\rho_y = 0.45\text{GPa}$ in this example) and the deviatoric stress, ρ , is given by

$$\rho = \sqrt{2J_2}, \quad J_2 = \frac{1}{2}\text{tr}([s][s]) \quad \text{where} \quad [s] = [\sigma] - \frac{I_1}{3}[I] \quad \text{and} \quad I_1 = \text{tr}([\sigma]).$$

$\text{tr}([\cdot])$ denotes the trace of $[\cdot]$ and $[I]$ is a three by three identity matrix. In principal stress space, this yield criterion defines an open-ended cylinder with a yield radius of ρ_y and its major axis aligned with the hydrostatic axis (the line where $\sigma_1 = \sigma_2 = \sigma_3$). See Coombs [4] for a full description of the adopted the elasto-plastic finite deformation framework.

Nagtegaal *et al.* [11] provided the small strain analytical limit load, controlled by a limiting stress at the notch of $\sigma_{\text{lim}} \approx 2.97\sigma_y$. The specimen modelled had a total height and width of 30mm and 10mm respectively, with a 2mm unit linking ligament at mid height. For this geometry, the small strain limit load is $F_{\text{lim}} \approx 2.673\text{kN}$. Due to symmetry, only one quarter of the specimen was discretised using seventy-five 20-noded hexahedral elements with a unit thickness, as shown in Figure 8. A displacement of $v = 0.2\text{mm}$ was applied in 40 equal displacement-controlled increments. The through-thickness faces of the elements were constrained perpendicular to the elevation shown in Figure 8. Note, that although this is a plane-strain situation, a three-dimensional analysis was performed to allow for more interesting mesh distortion to be applied.

The external load (total edge reaction) versus displacement response is shown by the black line in Figure 8 using an undistorted mesh of 20-noded elements with reduced 8 point quadrature. Note that full integration of the classical polynomial element produces an over-stiff response and fails to capture the presence of a limit load (for example, see [4] and the references contained therein). The predicted limit load is lower than that of the analytical small strain solution. This is due to the thickness of the ligament reducing as the deformation proceeds. This reduction in width concentrates the stress in the ligament, resulting in a lower peak force and a post-peak softening response not predicted by the small strain analysis. The three formulations gave indistinguishable results for the undistorted mesh, with a peak load of 2.397kN, as shown by the solid black line in Figure 8.

The finite-element mesh was distorted by translating each node not located on the x or y limits of the domain randomly by $\in [-0.2, 0.2]\text{mm}$ in both the x and y directions. A two-dimensional elevation of the distorted mesh is shown on the right of Figure 8 and three-dimensional wire-frame is shown inset on the load versus displacement curve. The distortion caused the volume associated with each of the Gauss points within the elements to vary between 0.036 and 0.274mm³, compared with a uniform constant of 0.125mm³ in the undistorted mesh.

As with the previous analysis on an elastic cantilever, distorting the mesh caused a

stiffening and softening of the PP and MM formulations, respectively. The PP simulation had a peak load of 2.463kN whereas the MM analysis peaked at 2.311kN. This variation is shown in Figure 8 by the dashed grey lines. The load versus displacement response of the PML formulation is indistinguishable from the undistorted curves and the maximum force exhibited only a 0.03% difference from the undistorted analysis maximum. This three-dimensional elasto-plastic finite deformation simulation demonstrates the ability of the PML formulation to provide mesh distortion resistant results compared to the classical PP and MM approaches.

5. Conclusion

This paper has proposed a new distortion resistant element formulation based on conventional polynomial test functions combined with novel local metric trial functions using a local convected coordinate system. The use of this local coordinate system has rendered the element rotationally invariant, overcoming one of the major inadequacies of the previous distortion immune formulations. The element was cast within a finite deformation framework. Its numerical performance has been demonstrated using a series of analyses, namely: (i) a linear elastic plane stress cantilever, (ii) a three-dimensional finite deformation patch test, (iii) a soft elastic cantilever beam, (iv) an eccentrically loaded column and (v) an elasto-plastic double-notched plate. The proposed element was shown to be rotationally invariant and have similar distortion resistance to existing unsymmetric formulations [12, 14, 16, 17, 18]. Although element formulations based on Airy stress functions [2, 3] have been shown to have superior distortion resistance, they can only be applied to a limited class of problems (currently, linear isotropic elasticity).

Previously, the unsymmetric nature of these distortion resistant elements has been criticised. However, setting the elements within a geometrically non-linear formulation removes this criticism due to the unsymmetric nature of the consistent material stiffness matrix. That is, even when the same test and trial functions are used the element stiffness matrix remains unsymmetric. These elements have the potential to perform well in simulating processes involving significant mesh distortion, helping delay the computationally expensive task of re-meshing. For any element to be used in general finite-element analysis, especially in the realm of finite deformation, it is essential that the formulation is invariant to the particular frame of reference. Therefore, the family of elements proposed in this paper provide an important step in overcoming the problem of mesh distortion sensitivity.

References

- [1] K.J. Bathe, E. Ramm, E. Wilson, Finite element formulations for large deformation dynamic analysis, *Int. J. Numer. Meth. Eng.* 9 (1975) 353–386.

- [2] S. Cen, X.R. Fu, G.H. Zhou, 8- and 12-noded plane hybrid stress-function elements immune to severely distorted mesh containing elements with concave shapes, *Comp. Methods Appl. Mech. Engng.* 200 (2011) 2321–2236.
- [3] S. Cen, G.H. Zhou, X.R. Fu, A shape-free 8-noded plane element usymmetric analytical trial function method, *Int. J. Num. Meth. Engng.* 91 (2012) 158–185.
- [4] W. Coombs, Finite deformation of particulate geomaterials: frictional and anisotropic Critical State elasto-plasticity, Ph.D. thesis, Durham University, 2011.
- [5] I. Fried, Possible loss of accuracy in curved (iso-parametric) finite elements, comments on a paper by henshell, *J. Sound Vib.* 23 (1972) 507–510.
- [6] R. Henshell, D. Walters, G. Warburton, On possible loss of accuracy in curved finite elements, *J. Sound Vib.* 23 (1972) 510–513.
- [7] D.N. Kim, F. Montáns, K. Bathe, Insight into a model for large strain anisotropic elasto-plasticity, *Comput. Mech.* 44 (2009) 651–668.
- [8] K. Liew, S. Rajendran, W. Wang, A quadratic plane triangular element immune to quadratic mesh distortions under quadratic displacement fields, *Comput. Methods Appl. Mech. Engrg.* 195 (2006) 1207–1223.
- [9] G.R. Liu, K.Y. Dai, T.T. Nguyen, A smoothed finite element method for mechanics problems, *Comput Mech* 39 (2007) 859–877.
- [10] T.K. Molstad, Finite deformation analysis using the finite element method, Ph.D. thesis, University of British Columbia, 1977.
- [11] J. Nagtegaal, D. Parks, J. Rice, On numerically accurate finite element solutions in the fully plastic range, *Comp. Methods Appl. Mech. Engng.* 4 (1974) 153–177.
- [12] E. Ooi, S. Rajendran, J. Yeo, 20-node hexahedral element with enhanced distortion tolerance, *Int. J. Numer. Methods Engrg* 60 (2004) 2501–2530.
- [13] E.T. Ooi, S. Rajendran, J.H. Yeo, Extension of unsymmetric finite elements us-quad8 and us-hexa20 for geometric nonlinear analyses, *Engineering Computations* 24(4) (2007) 407–431.
- [14] E.T. Ooi, S. Rajendran, J.H. Yeo, Remedies to rotational frame dependence and interpolation failure of us-quad8 element, *Communications in Numerical Methods in Engineering* 24 (2008) 1203–1217.
- [15] G. Prathap, V. Senthilkumar, S. Manju, Mesh distortion immunity of finite elements and the best-fit paradigm, *Sadhana* 31 (2006) 505–514.

- [16] S. Rajendran, A technique to develop mesh-distortion immune finite elements, *Comput. Methods Appl. Mech. Engrg.* 199 (2010) 1044–1063.
- [17] S. Rajendran, K. Liew, A novel unsymmetric 8-node plane element immune to mesh distortion under a quadratic displacement field, *Int. J. Numer. Methods Engrg.* 58 (2003) 1713–1748.
- [18] S. Rajendran, E. Ooi, J. Yeo, Mesh-distortion immunity assessment of quad8 elements by strong-form patch tests, *Commun. Numer. Methods Engrg.* 23 (2007) 157–168.
- [19] J. Simo, F. Armero, Geometrically non-linear enhanced strain mixed methods and the method of incompatible modes, *Int. J. Num. Meth. Engng.* 33 (1992) 1413–1449.
- [20] J. Simo, M. Rifai, A class of mixed assumed strain methods and the method of incompatible modes, *Int. J. Num. Meth. Engng.* 29 (1990) 1595–1638.
- [21] E. de Souza Neto, D. Perić, M. Dutko, D.R.J. Owen, Design of simple low order finite elements for large strain analysis of nearly incompressible solids, *Int. J. Solids Structures* 33 (1996) 3277–3296.
- [22] Z. Ullah, Nonlinear solid mechanics analysis using the parallel selective element-free Galerkin method, Ph.D. thesis, Durham University, 2013.
- [23] Z. Wei, D. Perić, D.R.J. Owen, Consistent linearization for the exact stress update of prandtl-reuss non-hardening elastoplastic models, *Int. J. Num. Meth. Engng.* 39 (1996) 1219–1235.

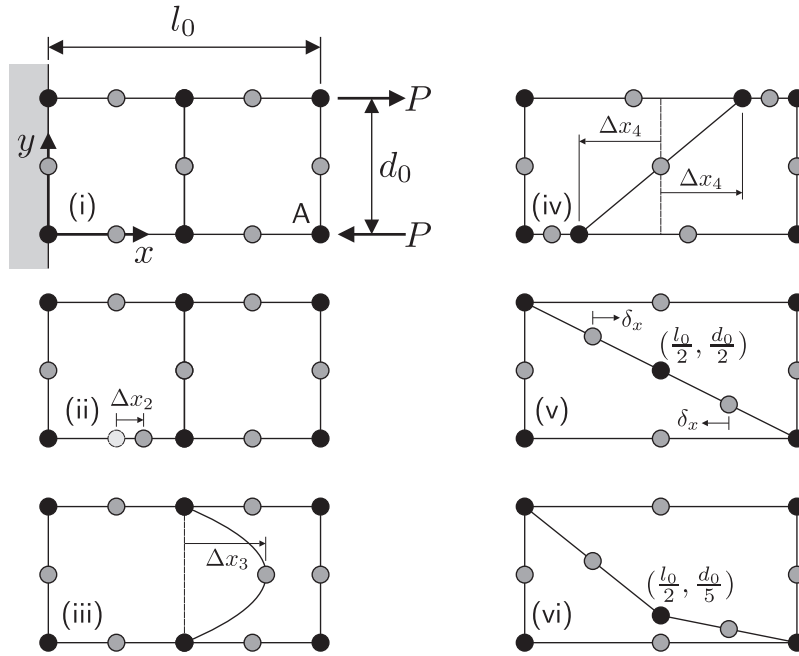


Figure 1: Plane stress linear elastic cantilever beam discretisations.

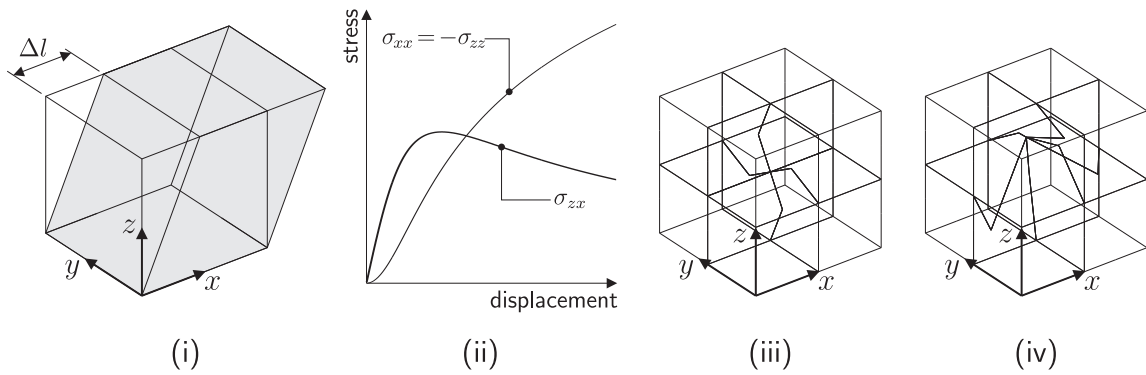


Figure 2: Simple shear patch test: (i) deformation, (ii) stress versus displacement response, (iii) rotational and (iv) random mesh distortion.

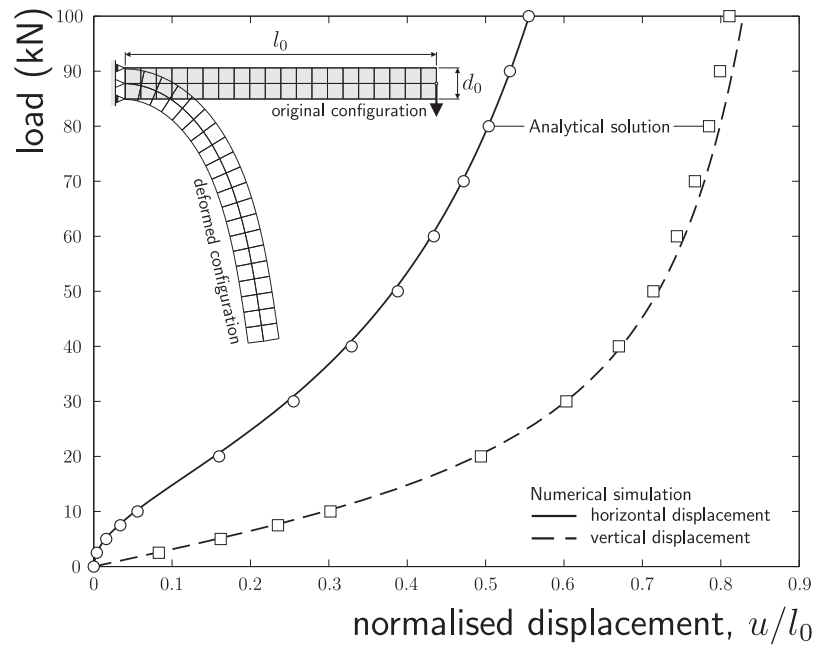


Figure 3: Two-dimensional elastic cantilever: force versus normalised displacement response for all element formulations and original/deformed undistorted discretisations and for the PM and PML distorted meshes.

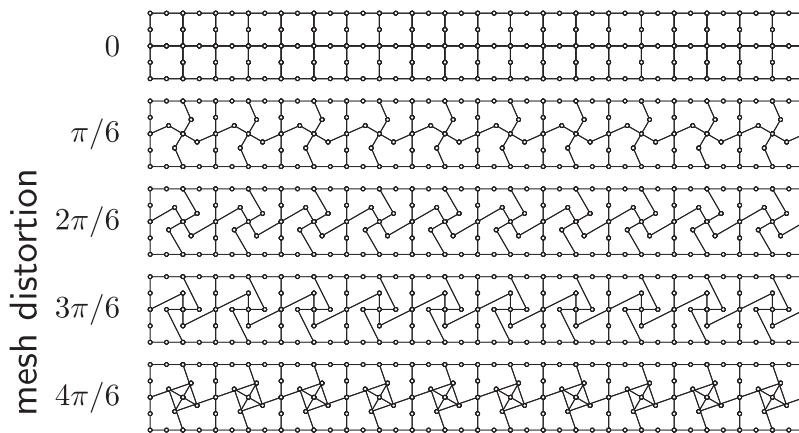


Figure 4: Two-dimensional elastic cantilever: mesh configurations.

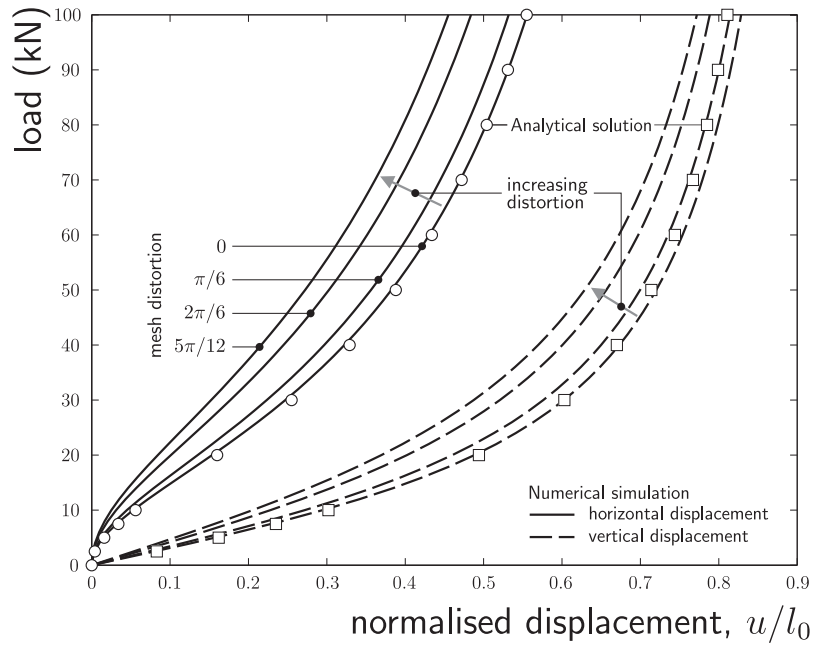


Figure 5: Two-dimensional elastic cantilever: force versus normalised displacement response for the PP formulation.

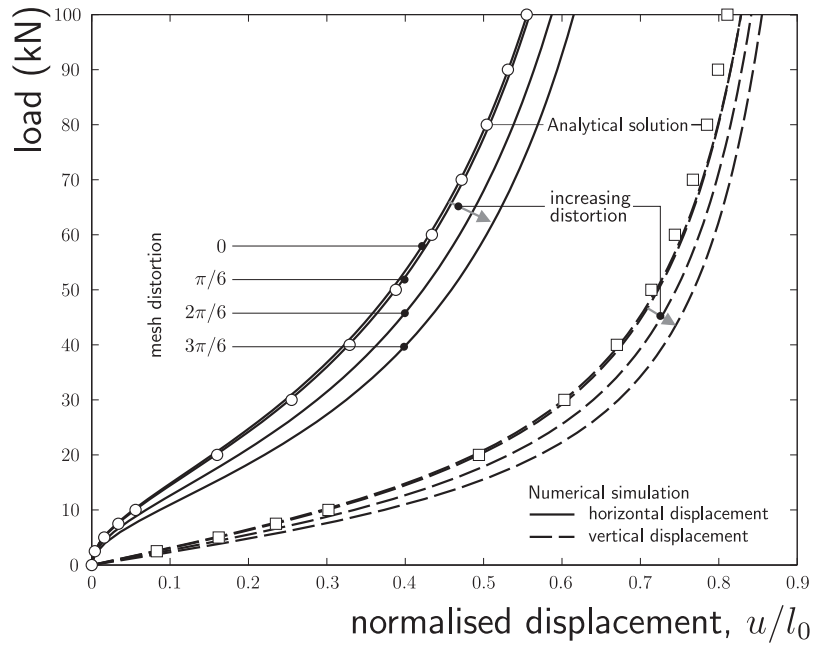


Figure 6: Two-dimensional elastic cantilever: force versus normalised displacement response for the MM formulation.

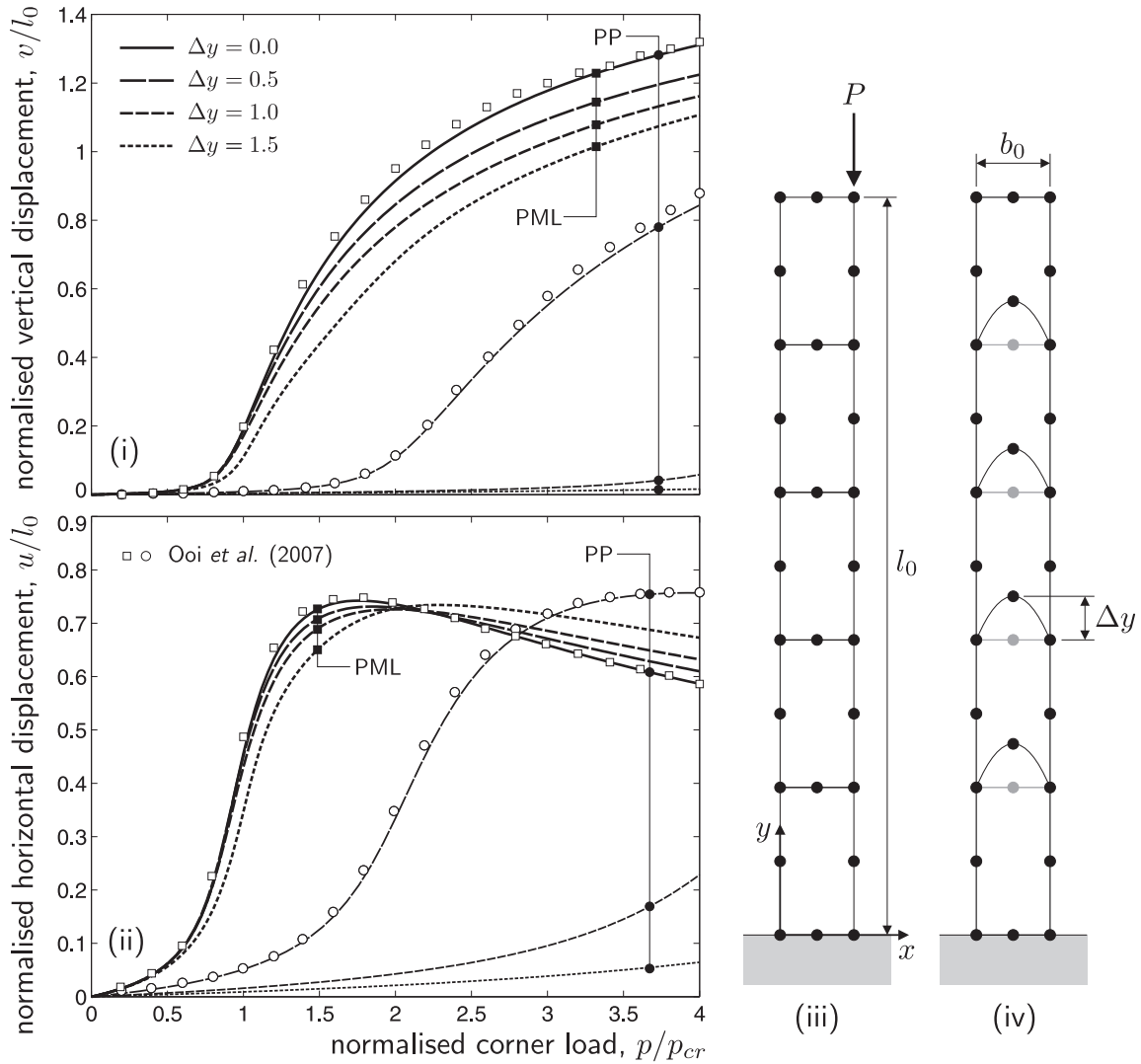


Figure 7: Buckling of a column under an eccentric load: normalised load versus (i) normalised vertical displacement and (ii) normalised horizontal displacement, (iii) uniform discretisation and (iv) distorted discretisation.

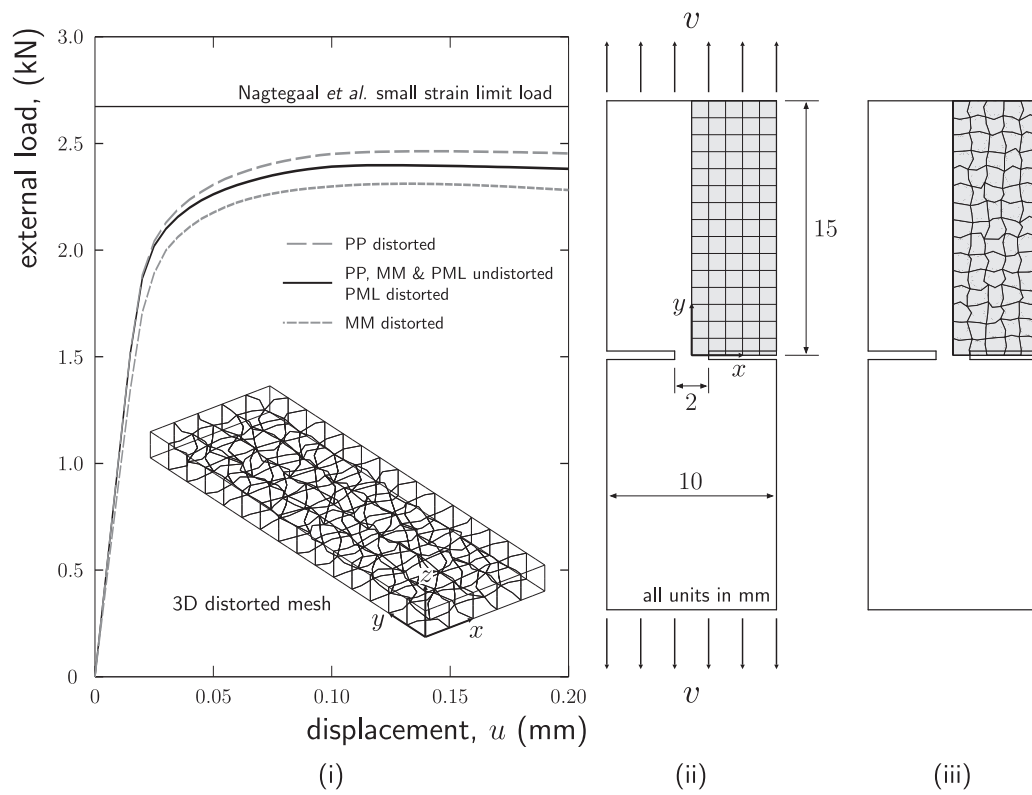


Figure 8: Finite deformation analysis of a double notched plate: (i) load versus displacement response, (ii) specimen dimensions and uniform discretisation and (iii) distorted mesh elevation.

mesh	rotation	PP	PM	PML	US-ATFQ8	HSF-Q8-15 β
(i)	0°	-2.11	-2.11	-2.11	1.30	0.01
	20°	-2.11	-2.07	-2.11	1.30	0.01
(ii)	0°	-3.20	-0.50	0.32	1.54	0.20
	20°	-3.20	-0.65	0.32	1.54	0.20
(iii)	0°	-43.81	-9.78	-10.37	-4.14	-6.48
	20°	-43.81	-9.81	-10.37	-4.14	-6.48
(iv)	0°	-3.80	-2.13	-2.14	1.43	0.01
	20°	-3.80	-2.07	-2.14	1.43	0.01
(v)	0°	-	-	6.70 [†]	1.95	0.10
	20°	-	-	6.70 [†]	1.95	0.10
(vi)	0°	-	-	37.81	1.71	-0.06
	20°	-	-	37.81	1.71	-0.06

Table 1: Plane stress linear elastic cantilever beam: displacement errors. [†] denotes a perturbed mesh result.

rotation	PML		PP		MM		PM	
	u/l_0	v/l_0	u/l_0	v/l_0	u/l_0	v/l_0	u/l_0	v/l_0
0	-0.554	-0.826	-0.554	-0.826	-0.554	-0.826	-0.554	-0.826
$\pi/6$	-0.552	-0.825	-0.532	-0.814	-0.559	-0.828	-0.553	-0.825
$2\pi/6$	-0.554	-0.826	-0.484	-0.789	-0.587	-0.841	-0.553	-0.825
$3\pi/6$	-0.554	-0.825	-	-	-0.615	-0.855	-0.553	-0.825
$4\pi/6$	-0.554	-0.825	-	-	-0.615	-0.856	-0.554	-0.826

Table 2: Two-dimensional elastic cantilever: normalised horizontal and vertical displacement with mesh distortion

global rotation	PML		PP		MM		PM	
	u/l_0	v/l_0	u/l_0	v/l_0	u/l_0	v/l_0	u/l_0	v/l_0
0	-0.554	-0.826	-0.484	-0.789	-0.587	-0.841	-0.553	-0.825
$\pi/12$	-0.554	-0.826	-0.484	-0.789	-0.579	-0.839	-0.552	-0.825
$2\pi/12$	-0.554	-0.826	-0.484	-0.789	-0.558	-0.828	-0.553	-0.826
$3\pi/12$	-0.554	-0.826	-0.484	-0.789	-0.577	-0.838	-0.556	-0.826
$4\pi/12$	-0.554	-0.826	-0.484	-0.789	-0.591	-0.845	-0.555	-0.827
$5\pi/12$	-0.554	-0.826	-0.484	-0.789	-0.594	-0.845	-0.553	-0.826
$6\pi/12$	-0.554	-0.826	-0.484	-0.789	-0.587	-0.841	-0.553	-0.825

Table 3: Two-dimensional elastic cantilever: normalised horizontal and vertical displacement with global mesh rotation with $2\pi/6$ mesh distortion